

SCIENTIFIC REPORTS



OPEN

Current-limiting challenges for all-spin logic devices

Li Su^{1,2,3,4}, Youguang Zhang^{1,2}, Jacques-Olivier Klein^{3,4}, Yue Zhang^{1,2}, Arnaud Bournel^{3,4}, Albert Fert^{1,2,5} & Weisheng Zhao^{1,2,3,4}

Received: 22 June 2015

Accepted: 11 September 2015

Published: 09 October 2015

All-spin logic device (ASLD) has attracted increasing interests as one of the most promising post-CMOS device candidates, thanks to its low power, non-volatility and logic-in-memory structure. Here we investigate the key current-limiting factors and develop a physics-based model of ASLD through nano-magnet switching, the spin transport properties and the breakdown characteristic of channel. First, ASLD with perpendicular magnetic anisotropy (PMA) nano-magnet is proposed to reduce the critical current (I_{co}). Most important, the spin transport efficiency can be enhanced by analyzing the device structure, dimension, contact resistance as well as material parameters. Furthermore, breakdown current density (J_{BR}) of spin channel is studied for the upper current limitation. As a result, we can deduce current-limiting conditions and estimate energy dissipation. Based on the model, we demonstrate ASLD with different structures and channel materials (graphene and copper). Asymmetric structure is found to be the optimal option for current limitations. Copper channel outperforms graphene in term of energy but seriously suffers from breakdown current limit. By exploring the current limit and performance tradeoffs, the optimization of ASLD is also discussed. This benchmarking model of ASLD opens up new prospects for design and implementation of future spintronics applications.

According to the well-known Moore's law, the development of electronic device is undergoing the bottleneck of the power and performance with continuous minimization^{1,2}. Spintronics manipulates the electron spin instead of charge as state variable for electrical information processing, which gives rise to the possibility of many applications such as ultra-low power logic and non-volatile storage³⁻⁶. Spintronics devices have been proposed to perform logic operations, but most of them suffer from the large dynamic power inherent in the magnetic field to be used or in the requirement to frequently transform data between electrical and magnetic states for pipeline computing⁷⁻⁹. All-spin logic device (ASLD) is one of the most promising candidates to overcome the above issues since it both stores and computes with spin information and logic-in-memory structure¹⁰. The essential physical basis of ASLD is nonlocal spin transfer torque (STT) effect^{11,12} attributing to pure spin injection and detection in the lateral nonlocal spin valve (LNLSV)¹³. This phenomenon has been observed experimentally in all-metal LNLSV¹⁴⁻¹⁷, generally copper is considered as typically channel material. Recently, a benchmarking methodology based on copper channel ASLD for computing system has been further introduced and simulated¹⁸. Furthermore, ASLD with perpendicular magnetic anisotropy (PMA) nano-magnet is suggested to lower STT switching critical current density^{18,19}. Nonetheless, with shrinking device dramatically, the current density challenges to exceeding the breakdown limit of copper due to electromigration (EM) crisis in 2015²⁰. For nanometer size ASLD, the breakdown characteristic of metal channel cannot be ignored and new material is also in great demand.

With the features of high electronic mobility, weak spin orbit coupling and hyperfine interactions, graphene has attracted considerable interests for future spintronics material²¹⁻²³. In addition, the

¹Fert Beijing Institute, Univ. Beihang, 100191, Beijing, China. ²School of Electrical & Information Engineering, Beihang Univ, Beijing 100191, Peoples R China. ³Institut d'Electronique Fondamentale, Univ. Paris-Sud, F-91405 Orsay, France. ⁴UMR 8622, CNRS, F-91405 Orsay, France. ⁵Unité Mixte de Physique CNRS-Thales, F-91767 Palaiseau, France. Correspondence and requests for materials should be addressed to W.Z. (email: weisheng.zhao@buaa.edu.cn)

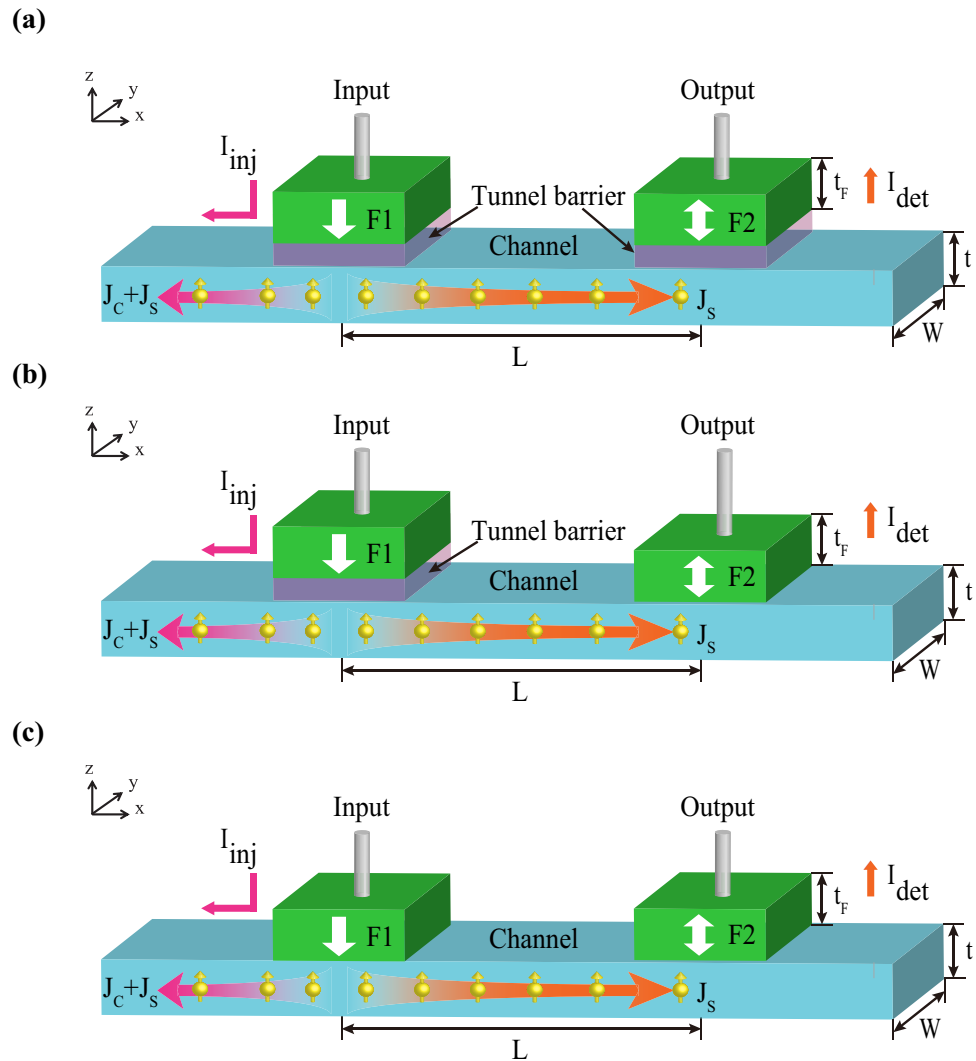


Figure 1. Main part of all-spin logic device (ASLD), i.e. structure of lateral nonlocal spin valve (LNLSV). (a) Structure with tunnel barrier contact in both the input and output F1/T/C/T/F2. (b) Structure with tunnel barrier contact in the input and transparent contact in the output F1/T/C/F2. (c) Structure with transparent contact both in the input and output F1/C/F2. J_s and J_c are spin current density and charge current density, respectively.

breakdown current density of graphene is at least two orders magnitude larger than that of copper^{24–27}. Moreover, nonlocal STT effect in graphene-based LNLSV has been experimental demonstrated^{28,29}, subsequently graphene-based all-spin logic gate (G-ASLG) with PMA nano-magnet has been proposed and evaluated¹⁹. However, the current-limiting factors of ASLD are lacking in detailed analysis, especially the current conditions, which is very important to assess the feasibility and optimization.

In this paper, we investigate the current-limiting factors of ASLD and develop a physics-based model including nano-magnet switching, spin transport properties and breakdown characteristic of channel. First, we present different structures of ASLD. Second, we introduce the compact model of ASLD based on STT effect in PMA nano-magnet, spin transport properties in LNLSV, and breakdown current density of channel, such as graphene and copper. Finally, we address the current-limiting conditions and energy dissipation to assess and optimize ASLD, which contributes to the design and implement of future spintronics devices.

Results and Discussions

All-spin logic device (ASLD). Firstly, as Fig. 1 shows, main part of ASLD is the structure of LNLSV, which is composed of PMA input and output nano-magnet (F1 and F2) connected by a nonmagnetic channel (such as copper or graphene). It is based on spin transport properties in LNLSV and nonlocal STT switching to perform logic operation. Once a charge current, I_{inj} , is injected into the device, spin current beneath input nano-magnet can diffuse in both directions, i.e., toward leftside (as a spin and

charge current) and toward rightside (as a pure spin current). Then a voltage V_{det} can be measured in the output nano-magnet as a result of spin accumulation in parallel (P) or antiparallel (AP) alignments of magnetizations, and the spin signal is defined as $R_s = (V_{det}^{AP} - V_{det}^P)/I_{inj}$. The spin current following into the output nano-magnet I_{det} is used to switch its magnetization based on nonlocal STT effect. Thus ASLD stores information as the magnetizations of input and output and communicates through pure spin current, just as its name implies.

To alleviate the conductance mismatch problem^{30–32} for graphene channel LNLSV, tunnel barrier has been added, seen in Fig. 1(a), to enhance the spin injection or detection efficiency $P_{1,2}$ and contribute to large spin signal R_s . Besides, asymmetric structure is presented as Fig. 1(b), where tunnel barrier is only added in the input. It can ensure high spin injection efficiency and large absorption with low contact resistance. For metal channel LNLSV or all-metal ASLD proposal, the transparent contact is generally used instead of tunnel barrier, as shown in Fig. 1(c). In the following, the performance of current-limiting and energy with these three structures are compared and discussed.

Current-limiting Models of ASLD. Afterwards, in order to study the current-limiting factors of the ASLD, we have developed a physics-based compact model that integrates STT switching of output nano-magnet, spin transport properties of LNLSV, and breakdown characteristic of channel. It allows us to analyze parameters such as device dimension, material parameters, and contact resistance and their interdependences, as well as to explore how to overcome current-limiting challenges and optimize ASLD performance.

Critical current of switching nano-magnet. Firstly, compared to in-plane magnetic anisotropy, PMA nano-magnet can reduce critical current density J_{c0} or current I_{c0} due to absence of the easy-plane anisotropy term¹¹. Therefore we consider ASLD with PMA nano-magnet so as to reduce required current essentially. In addition, the perpendicular anisotropy energy density K_{\perp} of PMA is high enough to ensure high thermal stability $\Delta = E_b/k_B T$, where E_b , k_B , T are energy barrier, Boltzmann constant and temperature, respectively. Regarding the nano-magnet size below the domain wall width, we assume single-domain magnetization reversal with STT effect^{12,13,33}. Since size effect of demagnetization factors is considered based on macrospin model³³, J_{c0} for PMA output nano-magnet can be derived as follows

$$J_{c0} = \frac{4e\alpha_{eff}E_b}{\hbar P A_c} = \frac{4e\alpha_{eff}K_{eff}t_F}{\hbar P} = \frac{2\alpha_{eff}e(2K_{\perp} - N_z\mu_0 M_s^2)t_F}{\hbar P} \quad (1)$$

where M_s is saturation magnetization and P is spin polarization factor. A_c is nano-magnet area and t_F is free layer thickness of output nano-magnet. e , \hbar , μ_0 are the elementary charge, reduced Planck constant and vacuum permeability, respectively. The demagnetization factors N_z is calculated to decrease with shrinking the nano-magnet size³⁴, consequently it enhances the effective perpendicular energy density $K_{eff} = K_{\perp} - N_z\mu_0 M_s^2/2$ shown in Fig. 2(a). Satisfying that J_{c0} is independent of nano-magnet area or only depends on nano-magnet thickness in the macrospin model³³, we can obtain effective damping constant α_{eff} shown in Fig. 2(a). Then the time-dependent magnetization dynamic is governed by the Landau-Lifshitz-Gilbert equation including spin torque^{11,12}. As a result, we give static and dynamic properties of switching output nano-magnet with scaling down (nano-magnet width W from 30 nm to 4 nm) in Fig. 2. It shows that thermal stability Δ scales almost linearly with nano-magnet width W , but critical current I_{c0} decreases in proportion to nano-magnet area A_c , leading to increasing STT efficiency Δ/I_{c0} with shrinking nano-magnet. The above modified macrospin model is able to demonstrate STT behavior with size effect, whose theoretical results agree well with experimental observations^{33,35}. Note that, as shown in Fig. 3(c), the critical current for required switching time 2 ns, $I_{tsw=2ns}$, which is equal to $I_{det, tsw=2ns}$, is utilized to further estimate the performance of ASLD in this paper.

Spin transport properties of ASLD. Most importantly, spin transports properties are figured out to diminish input charge current I_{inj} that generates I_{det} . Based on spin-dependent and one-dimensional drift-diffusion theory, we define and calculate spin transport efficiency η as^{13,19}

$$\eta \equiv I_{det}/I_{inj} = 2e^{-L/\lambda_N} \left(\frac{P \frac{R_1}{R_N}}{1 - P_1^2} + \frac{P \frac{R_F}{R_N}}{1 - P^2} \right) \times \left[\prod_{i=1}^2 \left(1 + \frac{2 \frac{R_i}{R_N}}{1 - P_i^2} + \frac{2 \frac{R_F}{R_N}}{1 - P^2} \right) - e^{-2L/\lambda_N} \right]^{-1} \quad (2)$$

where $R_F = \rho_F \lambda_F / (t_F A_C)$ is nano-magnet spin resistance with spin diffusion length λ_F , resistivity ρ_F , thickness t_F and contact or nano-magnet area A_C . $R_N = \rho_N \lambda_N / t_N W$ is spin resistance of nonmagnetic channel, where ρ_N , W , t_N and λ_N are the resistivity, width, thickness and spin diffusion length of channel, respectively. R_i is contact resistance of the injector ($i=1$) or the detector ($i=2$). P and P_i are the spin polarization of the electrode and the interfaces, respectively. Eq. (2) and Fig. 3 show that spin transport efficiency η depends strongly on the material parameters (R_i , P_i , λ_N) as well as the device geometry (channel width W and length

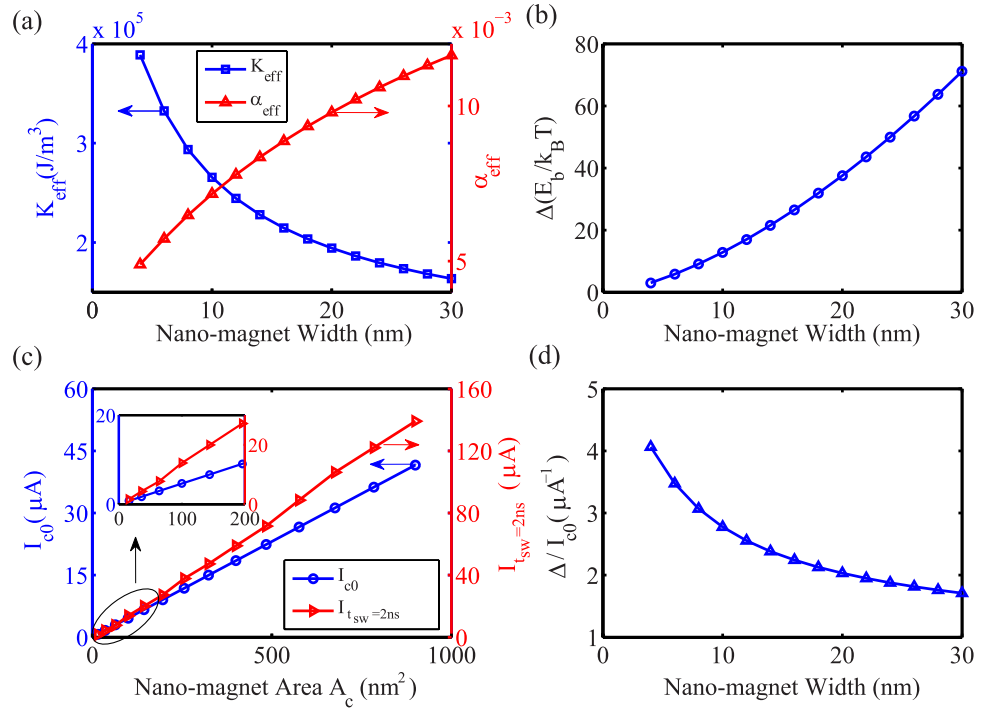


Figure 2. Static and dynamic properties for switching the output nano-magnet. The critical current density J_{c0} is calculated as 4.68 MA/cm^2 based on Eq. (1), and all the used parameters are listed in the Table 1. (a) Calculated effective perpendicular magnetic anisotropy energy density K_{eff} and effective damping constant α_{eff} as a function of nano-magnet width W . (b) Thermal stability Δ with respect to nano-magnet width W . (c) Calculation of the critical current I_{c0} and current for 2 ns switching time $I_{t_{\text{sw}}=2\text{ns}}$ as a function of square nano-magnet area A_c . (d) The dependence of spin-torque switching efficiency Δ/I_{c0} on nano-magnet width W .

L shown in Fig. 1). Especially, as shown in Fig. 2 (a), higher efficiency can be obtained by increasing input contact resistance R_1 and decreasing output contact resistance R_2 , thus asymmetric structure (as Fig. 1(b)) is expected. Note that, R_1W type of contact resistivity is generally utilized for graphene instead of R_1A type³⁶. According to nano-magnet switching and spin transport properties of channel, the lower limit of I_{inj} for workable ASLD is deduced as I_{c0}/η .

Breakdown current density of ASLD. Furthermore, with the object of finding the upper limit of I_{inj} of ASLD, we study the breakdown current density of channel J_{BR} . In this work, we focus on typically spin channel materials, graphene and copper. For graphene channel due to Joule heating mechanism, we apply the size-dependent model of Liao *et al.*³⁷ Taking into account both heat loss to the substrate and to the interface, the breakdown current density of graphene channel $J_{BR,G}$ is calculated as³⁷

$$J_{BR,G} = \left[\frac{g(T_{BD} - T_0)}{\rho_G t_G W} \times \frac{\cosh\left(\frac{L}{2L_H}\right) + gL_H R_T \sinh\left(\frac{L}{2L_H}\right)}{\cosh\left(\frac{L}{2L_H}\right) + gL_H R_T \sinh\left(\frac{L}{2L_H}\right) - 1} \right]^{1/2} \quad (3)$$

In our calculation, T_{BD} is the breakdown temperature ($\sim 873 \text{ K}$ oxidation in air); T_0 is ambient temperature (295 K); $L_H = \sqrt{k_G W t_G / g}$ is thermal healing length, k_G is thermal conductivity of graphene, and R_T is the thermal resistance at the metal contacts. The thermal contact resistance per unit length from the graphene channel to substrate is calculated as³⁷

$$g^{-1} = \left\{ \frac{\pi k_{ox}}{\ln[6(t_{ox}/W + 1)]} + \frac{k_{ox}}{t_{ox}} W \right\}^{-1} + \frac{R_{Cox}}{W} \quad (4)$$

Where k_{ox} is the thermal conductivity of substrate; t_{ox} is the thickness of substrate; R_{Cox} is thermal resistance of the graphene-substrate interface. Taking graphene-SiO₂ as example based on above model and experimental results²⁷, we require lower resistivity, smaller dimension and thinner substrate for higher $J_{BR,G}$ as illustrated in Fig. 4. Based on Eq. (3) and Eq. (4), higher thermal conductivity (k_{ox}) or lower

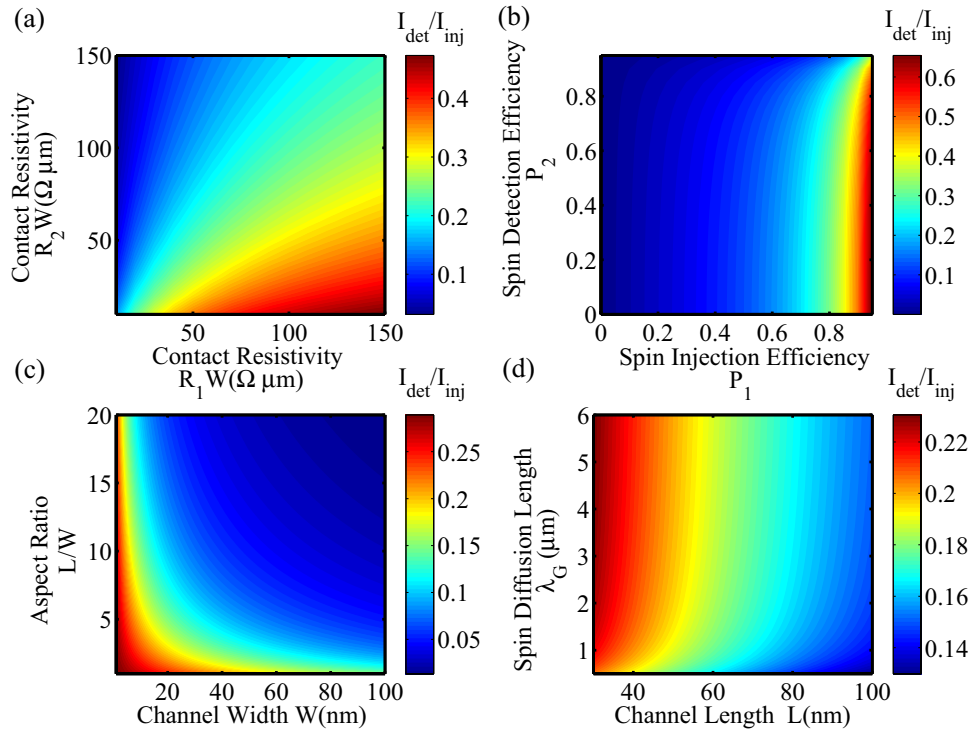


Figure 3. Calculation of spin transport efficiency I_{det}/I_{inj} of ASLD with graphene channel based on Eq. (2). The default device geometry is $(W, L) = (30 \text{ nm}, 100 \text{ nm})$, and the other parameters of graphene are listed in Table 1. (a) Calculation of I_{det}/I_{inj} as a function of contact resistivity $R_1 W$ and $R_2 W$. (b) Calculation of I_{det}/I_{inj} as a function of spin injection/detection efficiency P_1 and P_2 . (c) Calculation of I_{det}/I_{inj} as a function of device geometry (W, L) . (d) Calculation of I_{det}/I_{inj} as a function of diffusion length of graphene λ_G .

thermal resistance of graphene-substrate interface (R_{Cox}) can achieve higher breakdown current density. It is a possible solution to utilizing diamond substrates (higher k_{ox}) or graphene-BN substrates (lower R_{Cox} due to smoother interface).

Going forward metal channel, electromigration (EM) is one of the key current density limitations with shrinking size of device rapidly. We consider EM-failure mechanism for size-dependent breakdown current density of copper channel $J_{BR, Cu}$ with Blech model, and the threshold product is described as^{38,39}

$$(J_{BR, Cu} \times L)_{th} = \frac{\Omega \Delta \sigma}{Z^* e \rho_{Cu}} \quad (5)$$

where Ω , $\Delta \sigma$, Z^* are the atomic volume of copper, the normal stress difference between channel ends, and effective charge of copper. The threshold product can be obtained experimentally, for example, 1500 A/cm for Cu/SiO₂, then the length-effect design can be realized. Furthermore, the increasing resistivity of copper ρ_{Cu} with narrow-width effect is also under consideration⁴⁰, resulting in decreasing $J_{BR, Cu}$ based on Eq. (5). Therefore calculated $J_{BR, Cu}$ with size-effect are presented in Fig. 4(c,d). It shows that, $J_{BR, Cu}$ will suffer from the great growing resistivity and benefit from the short-length effect. In contrast, graphene can sustain current density around 10¹⁰ A/cm², 2 orders of magnitude higher than that of copper.

Current-limiting conditions and optimization. Finally, the whole current-limiting factors have been investigated as above, namely the current-limiting conditions of ASLD can be written as following,

$$I_{c0}/\eta \leq I_{inj} \leq I_{BR} = J_{BR} \times A_c \quad (6)$$

Given a workable injection current I_{inj} , we can obtain its switching time t_{sw} by solving LLG equation. Note that the process time of ASLD is determined by the STT switching, and the time of spin current propagation is ignored^{2,41}. To demonstrate the entire performance of ASLD, the device energy dissipation per bit can be estimated as

$$E = I_{inj}^2 \times R_{in} \times t_{sw} \quad (7)$$

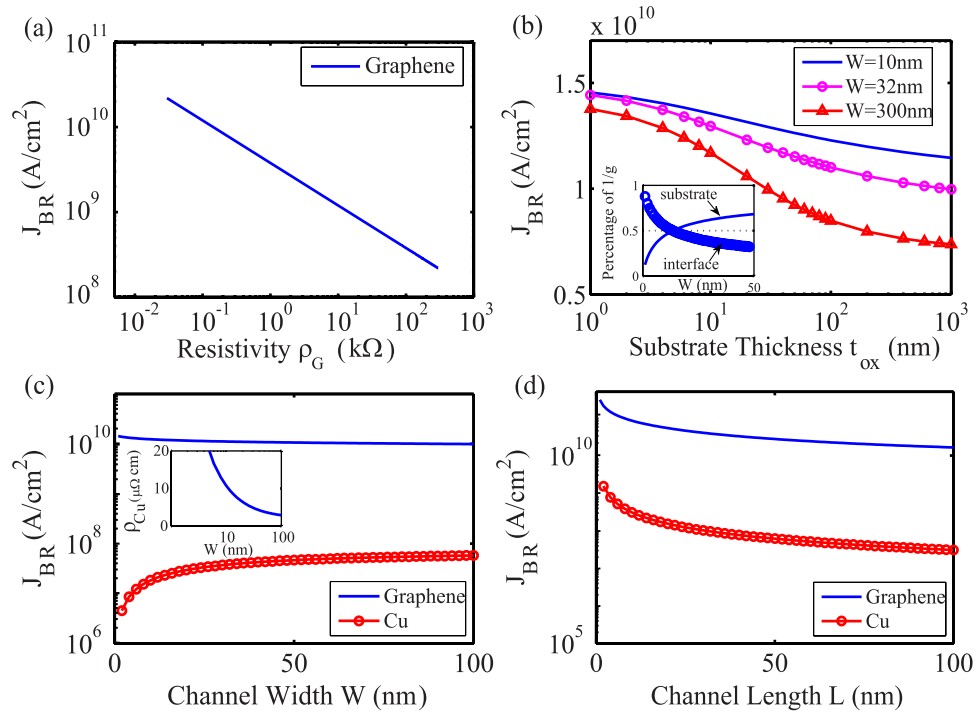


Figure 4. Breakdown current density J_{BR} of graphene and copper. (a) The breakdown current density vs resistivity for $32 \text{ nm} \times 80 \text{ nm}$ ($W \times L$) graphene channel on 90 nm thickness SiO_2 . Thermal conductivity of graphene and SiO_2 are $k_G = 100 \text{ W} \cdot \text{m}^{-1} \cdot \text{K}^{-1}$ and $k_{ox} = 1.4 \text{ W} \cdot \text{m}^{-1} \cdot \text{K}^{-1}$, respectively. Graphene-oxide interface thermal resistance $R_{cox} = 10^{-8} \text{ m}^2 \text{ K W}^{-1}$. (b) Calculated dependence of J_{BR} on oxide thickness t_{ox} and graphene channel width W based on Eqs. (3 and 4). The inset shows that percentage of contribution to total thermal resistance (g^{-1}) from the graphene-oxide interface and substrate, as a function of graphene channel width at $t_{ox} = 90 \text{ nm}$. Parameters used are same as above. (c) Calculated dependence of J_{BR} as a function of channel width. $L = 100 \text{ nm}$, and the other parameters are same as Table 1. The inset shows the resistivity of copper will dramatically increase for sub-100 nm wide based on Eq. (11), resulting in the decrease of $J_{BR, Cu}$ based on Eq. (5). (d) Calculated dependence of J_{BR} as a function of channel length.

where R_{in} ($\sim R_I$) is input resistance related to the input charge current path. Based on Eq. (2), as contact resistance R_I increases, spin transport efficiency η is higher, which can reduce injection current I_{inj} so as to help lower energy. However, the increase of R_I leads to the augmentation of energy. Thus contact resistance R_I has optimal value for the minimum energy of ASLD. As mentioned, the LLG solution value of $I_{det, tsW=2ns}$ for nano-magnet $W = 10 \text{ nm}$, $t_F = 2 \text{ nm}$ is taken into account. Figure 5 shows the injection current and energy as a function of contact resistance for both graphene and copper channel in different lengths L , the breakdown current is also illustrated as the upper limitation. In Fig. 5(a) and Fig. 5(c), the injection current I_{inj} exhibits a minimum, since increasing R_I will reduce η and boost I_{inj} after the saturation of spin signal R_s with $R_I \gg R_N$. The advantage of the breakdown current density of graphene makes a broad workable current range for ASLD, that is to say, we can enhance injection current I_{inj} for fast speed $1/t_{sw}$. But it is true that the spin resistance of graphene R_G is larger than that of copper, the optimal contact resistance of graphene channel corresponds to be larger. As shown in Fig. 5(b) and Fig. 5(d), the optimized energy of graphene channel ASLD is almost ten times larger than that of copper channel ASLD. In addition, it is found that the optimal value of contact resistance increases as the channel length.

At last, we have demonstrated and analyzed all the performances of ASLD in different materials (graphene and copper) and structures as shown in Fig. 6. The dependence of each parameter is analyzed. Thanks to spin transport efficiency, asymmetric structure is the optimal structure for lower injection current I_{inj} to overcome current-limiting issue. To reduce injection current and energy dissipation in the same structure, smaller device with larger aspect ratio W/L , higher spin injection efficiency P_I , and longer diffusion length λ_N are expected. For the copper channel, the device geometry and material parameters are strictly satisfied due to the breakdown current. For example, if we take 10 nm wide copper channel with both transparent contacts, F1/Cu/F2, breakdown will always occur unless the channel length L is within 20 nm as shown in Fig. 6(a). Even so, the required spin injection efficiency must reach up to 0.5 at least and the minimal spin diffusion length is 200 nm . Compared with copper, graphene can sustain higher breakdown current so that it can easily obtain an achievable ASLD. However, the energy performance of graphene channel ASLD is restricted by its large contact resistance. It is a possible solution to finding new tunnel material that realizes lower contact resistance as well as high efficiency.

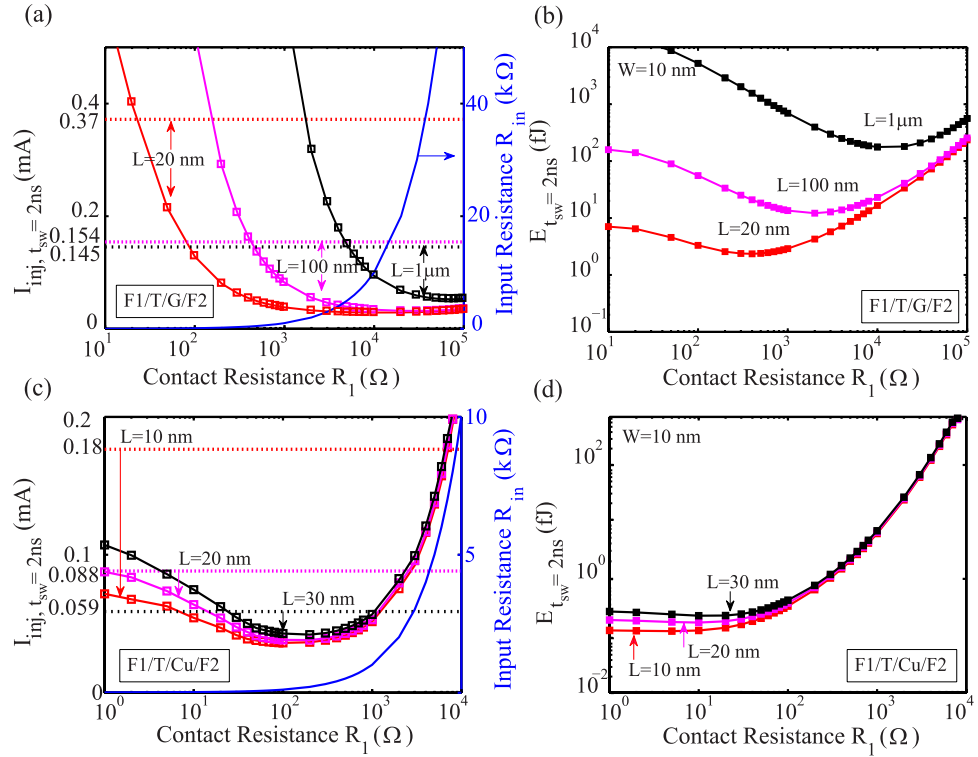


Figure 5. Analysis and optimization of injection current and energy based on contact resistance. (a) Calculated injection current I_{inj} for switching time $t_{sw} = 2$ ns, $I_{inj, t_{sw}=2ns}$ and input resistance R_{in} as a function of contact resistance R_1 at different values of channel length for structure F1/T/G/F2. The dash line stands for the corresponding breakdown current density $J_{BR, G}$. (b) Calculated energy for switching time $t_{sw} = 2$ ns, $E_{t_{sw}=2ns}$ as a function of contact resistance R_1 at different values of channel length for structure F1/T/G/F2. (c) Calculated $I_{inj, t_{sw}=2ns}$ and R_{in} as a function of contact resistance R_1 at different values of channel length for structure F1/T/Cu/F2. $J_{BR, Cu}$ is illustrated as dash line. (d) Calculated $E_{t_{sw}=2ns}$ as a function of contact resistance R_1 at different values of channel length for structure F1/T/Cu/F2.

Conclusions

In summary, we have developed a physic-based model for ASLD including PMA nano-magnet switching, spin transport properties and breakdown characteristic of channel. Its current-limiting factors, i.e., critical current of nano-magnet, spin transport efficiency and breakdown current of channel, have been investigated. In order to estimate the feasibility and performance of ASLD, the current-limiting conditions and energy dissipation have been addressed. Moreover, it has been shown that the contact resistance can be optimized for minimum energy. Regardless of the spin channel materials, the asymmetric structure is the most effective for ASLD in terms of current limitation. Copper channel outperforms graphene in term of energy but seriously suffers from the breakdown current limit. By exploring the current limit and performance tradeoffs, we can expect larger aspect ratio W/L , higher spin injection efficiency P_I and longer diffusion length λ_N . Our work is significant in the design and implementation of reduced ASLD facing current-limiting challenges, which gives a promising prototype for future spintronics applications.

Methods

Statistic and dynamic model of switching nano-magnet. Spin transfer torque (STT) effect is simulated based on the model deriving from Slonczewski and Berger^{11,12}. The critical current density (J_{co}) and switching time (t_{sw}) for PMA nano-magnet vector (\vec{m}) have been calculated by following macrospin model based on Landau-Lifshitz-Gilbert (LLG) equation with STT term. The main parameters are described and listed in Table 1. J_{co} is given as Eq. (1), and the LLG equation reads

$$\frac{(1 + \alpha_{\text{eff}}^2)}{\gamma} \frac{\partial \vec{m}}{\partial t} = -\mu_0 \vec{m} \times \vec{H}_{\text{eff}} - \alpha_{\text{eff}} \mu_0 \vec{m} \times (\vec{m} \times \vec{H}_{\text{eff}}) - \gamma a_J \vec{m} \times (\vec{m} \times \vec{p}) + \alpha_{\text{eff}} a_J (\vec{m} \times \vec{p}) \quad (8)$$

where a_J is the strength of spin transfer torque, $a_J = \hbar P J / 2e M_s t_F$, J is the current density, and p is a unit vector representing the direction of the magnetization of the input nano-magnet. As the size of device

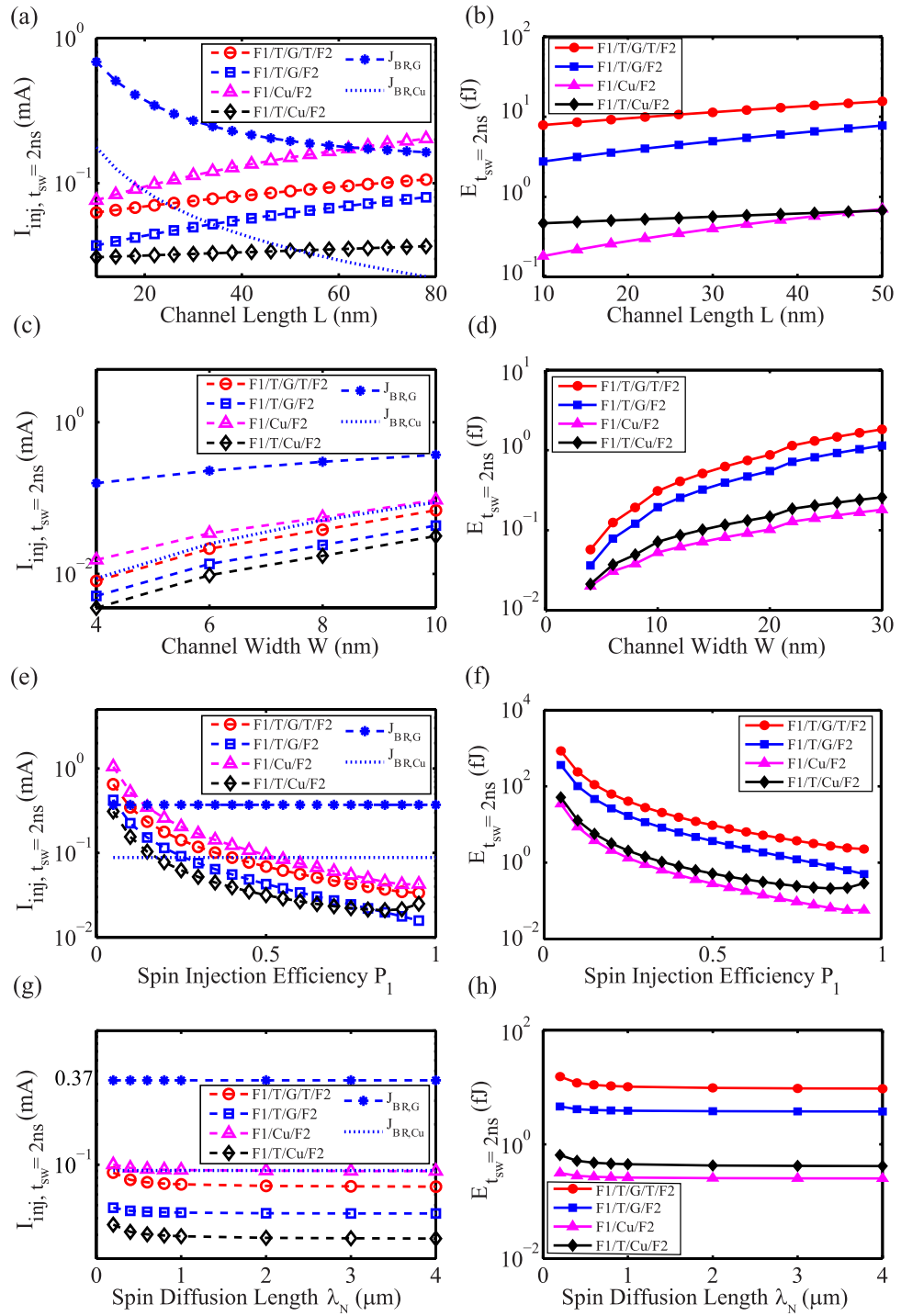


Figure 6. Calculated injection current I_{inj} and energy for switching time $t_{sw} = 2$ ns in different materials and structures considering the breakdown current density J_{BR} . The transparent contact resistivity of copper channel is used as $R_c A = 0$, and the other default parameters are listed in Table 1. **(a,b)** give the calculated dependence $I_{inj, t_{sw}=2ns}$ and $E_{t_{sw}=2ns}$ on channel length L . **(c,d)** give the calculated dependence $I_{inj, t_{sw}=2ns}$ and $E_{t_{sw}=2ns}$ on channel width W . **(e,f)** give the calculated dependence $I_{inj, t_{sw}=2ns}$ and $E_{t_{sw}=2ns}$ on spin injection efficiency P_1 . **(g,h)** give the calculated dependence $I_{inj, t_{sw}=2ns}$ and $E_{t_{sw}=2ns}$ on spin diffusion length λ_N .

shrinks, we consider the nano-magnet width W smaller than the domain wall width (e.g. 30 nm^{35}) and assume that single-domain magnetization reversal takes place. Providing that interfacial and bulk magnetic anisotropies are intact, the effective perpendicular anisotropy field is expressed as

Parameter	Description	Default value
M_s	Saturation magnetization	9.5×10^5 A/m
K_{\perp}	Perpendicular magnetic anisotropy energy density	6.4×10^5 J/m ³
t_F	Free layer thickness of output nano-magnet	2 nm
W, L, t	Width, length and thickness of channel	10 nm, 20 nm, $t_G = 0.335$ nm
AR, TR	Aspect Ratio $L/W, t/W$	2, 6/5 (copper)
A_C	Nano-magnet area and contact area	10×10 nm ²
α_{eff}	Effective damping constant	0.007
N_x, N_y, N_z	Demagnetization factors	0.17, 0.17, 0.66 ^a
P	Spin polarization factor	0.5
P_i	Spin injection ($i=1$) or detection ($i=2$) efficiency	50% (0 ~ 100%)
$\lambda_G, \lambda_{Cu}, \lambda_F$	Spin diffusion length of graphene, copper and ferro nano-magnet	3 μ m, 400 nm, 5 nm
$\rho_{Cu,bulk}, \rho_G, \rho_F$	Resistivity of bulk copper, graphene channel and nano-magnet	1.7 $\mu\Omega$ ·cm, 0.3 k Ω ^b , 20 $\mu\Omega$ ·cm
$R_i \cdot W$	Contact resistivity for graphene channel in the input ($i=1$) or the output ($i=2$)	10 Ω · μ m (Tunnel), 1 Ω · μ m (Transparent)
$R_i \cdot A$	Tunnel contact resistivity for copper channel	0.02 Ω · μ m ²
Constant	Description	Value
\hbar	Reduced Planck constant	1.054×10^{-34} J·s
e	Elementary charge	1.6×10^{-19} C
μ_0	Vacuum permeability	1.2566×10^{-6} H/m
γ	Gyromagnetic ratio	1.76×10^{11} rad·s ⁻¹ ·T ⁻¹

Table 1. Main parameters for Calculation. ^aCalculated from W and t_F ³⁴. ^bNormalized by t_G .

$$\vec{H}_{eff} = (-N_x M_S, -N_y M_S, 2K_{\perp}/\mu_0 M_S - N_z M_S) \cdot \vec{m} \quad (9)$$

where N_x, N_y, N_z are demagnetization factors, which depend on the nano-magnet dimensions and satisfy that $N_x + N_y + N_z = 1$ ³⁴. As a result, the effective perpendicular anisotropy energy density $K_{eff} = K_{\perp} - N_z \mu_0 M_S^2/2$ increases with decreasing W owing to decrease of N_z ³⁴. Supposing that critical current density only relies on the material parameters and thickness of nano-magnet, we can obtain the calculated effective damping constant that reduces with W below 30 nm.

In addition, the disturbance caused by thermal agitation during the magnetization switching is supposed to be negligible, but the initial position of the nano-magnet vector is thermally distributed at a finite temperature. Here we use root square average value calculated by Eq. (10) as an initial angel θ

$$\langle \theta_0 \rangle = \sqrt{k_B T / (\mu_0 M_S H_{eff} V)} \quad (10)$$

In this work, we simulated time-dependent magnetization dynamics of 2-nm-thick nano-magnet width of 4 nm~30 nm by solving LLG equation and obtained the different critical current density or current for required switching time, e.g. $I_{tsw=2ns}$.

Spin transport model of LNLSV. The lateral non-local spin valve (LNLSV) is the key element of the ASLD. Aimed at the spin transport efficiency $\eta \equiv I_{det}/I_{inj}$, we analyzed the interface effects and spin accumulation based on the spin transport model of Takahashi¹³, taking into account the spin dependent and the one-dimensional drift-diffusion theory.

Physical model of copper resistivity. Regarding surface scattering of the conduction electrons and scattering due to grain boundaries, the resistivity is calculated as follows⁴¹

$$\rho_{Cu} = \rho_{Cu,bulk} \left\{ \frac{1}{3} \sqrt{\frac{1}{3} - \frac{\chi}{2} + \chi^2 - \chi^3 \ln \left(1 + \frac{1}{\chi} \right)} \right. \\ \left. + \frac{3}{8} C (1 - p) \frac{1 + TR}{TR} \frac{\lambda_{m,Cu}}{W} \right\}$$

with $\chi = \lambda_{m,Cu} Q / d (1 - Q)$ (11)

where p , Q , $\lambda_{m,Cu}$, d is the specularly parameter, the reflectivity coefficient at grain boundaries, the mean free path and the average distance between grain boundaries, respectively. C is a constant with value 1.2 for rectangular cross section channel. The parameters are set as $p = 0.49$, $Q = 0.27$, $\lambda_{m,Cu} = 45$, $d = 80$ nm and the others are listed in Table 1.

References

1. Taur, Y., Buchanan, D. A., Chen, W. *et al.* CMOS scaling into the nanometer regime. *Proc. IEEE*, **85**(4), 486–504 (1997).
2. Kim, N. S., Austin, T., Baauw, D. *et al.* Leakage current: Moore's law meets static power. *IEEE Computer*, **36**(12), 68–75 (2003).
3. Wolf, S. A. *et al.* Spintronics: a spin-based electronics vision for the future. *Science*, **294**, 1488–1495 (2001).
4. Žutić, I., Fabian, J. & Sarma, S. D. Spintronics: Fundamentals and applications. *Rev. Mod. Phys.* **76**, 323 (2004).
5. Chappert, C., Fert, A. & Van Dau, F. N. The emergence of spin electronics in data storage. *Nature Mater.* **6**, 813–823 (2007).
6. ITRS 2010 System Driver Update, ITRS 2011 Emerging Research Devices.
7. Xu, P. *et al.* An all-metallic logic gate based on current-driven domain wall motion. *Nature Nanotech.* **3**, 97–100 (2008).
8. Dery, H., Dalal, P., Cywinski, L. & Sham, L. J. Spin-based logic in semiconductors for reconfigurable large-scale circuits. *Nature*, **447**, 573–576 (2007).
9. Leem, L. & Harris, J. S. Magnetic coupled spin-torque devices for nonvolatile logic applications. *J. Appl. Phys.* **105**, 07D102 (2009).
10. Behin-Aein, B., Datta, D., Salahuddin, S. & Datta, S. Proposal for an all-spin logic device with built-in memory. *Nature Nanotech.* **5**, 266–270 (2010).
11. Slonczewski, J. C. Current-driven excitation of magnetic multilayers. *J. Magn. Magn. Mater.* **159**, L1–L7 (1996).
12. Berger, L. Emission of spin waves by a magnetic multilayer traversed by a current. *Phys. Rev. B.* **54**, 9353 (1996).
13. Takahashi, S. & Maekawa, S. Spin injection and detection in magnetic nanostructures. *Phys. Rev. B.* **67**, 052409 (2003).
14. Jedema, F. J., Filip, A. T. & Van Wees, B. J. Electrical spin injection and accumulation at room temperature in an all-metal mesoscopic spin valve. *Nature*, **410**(6826), 345–348 (2001).
15. Jedema, F. J., Heersche, H. B. & Filip, A. T. *et al.* Electrical detection of spin precession in a metallic mesoscopic spin valve. *Nature*, **416**(6882), 713–716 (2002).
16. Kimura, T., Otani, Y. & Hamrle, J. Switching magnetization of a nanoscale ferromagnetic particle using nonlocal spin injection. *Phys. Rev. Lett.* **96**(3), 037201 (2006).
17. Fukuma, Y., Wang, L., Idzuchi, H. *et al.* Giant enhancement of spin accumulation and long-distance spin precession in metallic lateral spin valves. *Nature Mater.* **10**(7), 527–531 (2011).
18. Kim, J., Paul, A., Crowell, P. A. *et al.* Spin-Based Computing: Device Concepts, Current Status, and a Case Study on a Microprocessor. *Proc. IEEE*, **103**(1) (2015).
19. Su, L., Zhao, W., Zhang, Y. *et al.* Proposal for a graphene-based all-spin logic gate. *Appl. Phys. Lett.* **106**(7), 072407 (2015).
20. International Technology Roadmap for Semiconductor (ITRS). *International Technology Working Groups*. (<http://www.itrs.net>).
21. Geim, A. K. & Novoselov, K. S. The rise of graphene. *Nature Mater.* **6**, 183–191 (2007).
22. Han, W., McCreary, K. M., Pi, K. *et al.* Spin transport and relaxation in graphene. *J. Magn. Magn. Mater.* **324**, 369–381 (2012).
23. Han, W., Kawakami, R. K., Gmitra, M. *et al.* Graphene spintronics. *Nature Nanotech.* **9**(10), 794–807 (2014).
24. Murali, R., Yang, Y., Brenner, K. *et al.* Breakdown current density of graphene nanoribbons. *Appl. Phys. Lett.* **94**(24), 243114 (2009).
25. Yu, J., Liu, G., Sumant, A. V. *et al.* Graphene-on-diamond devices with increased current-carrying capacity: carbon sp²-on-sp³ technology. *Nano Lett.* **12**(3), 1603–1608 (2012).
26. Barreiro, A., Börrnert, F., Rummeli, M. H., *et al.* Graphene at high bias: Cracking, layer by layer sublimation, and fusing. *Nano Lett.* **12**(4), 1873–1878 (2012).
27. Behnam, A., Lyons, A. S., Bae, M. H. *et al.* Transport in nanoribbon interconnects obtained from graphene grown by chemical vapor deposition. *Nano Lett.* **12**(9), 4424–4430 (2012).
28. Lin, C. C., Penumatcha, A. V., Gao, Y. *et al.* Spin Transfer Torque in a Graphene Lateral Spin Valve Assisted by an External Magnetic Field. *Nano Lett.* **13**, 5177–5181 (2013).
29. Lin, C. C., Gao, Y., Penumatcha, A. V. *et al.* Improvement of Spin Transfer Torque in Asymmetric Graphene Devices. *ACS nano* (2014).
30. Schmidt, G. *et al.* Fundamental obstacle for electrical spin injection from a ferromagnetic metal into a diffusive semiconductor. *Phys. Rev. B.* **62**, R4790 (2000).
31. Rashba, E. I. Theory of electrical spin injection: Tunnel contacts as a solution of the conductivity mismatch problem. *Phys. Rev. B.* **62**, R16267 (2000).
32. Fert, A., & Jaffres, H. Conditions for efficient spin injection from a ferromagnetic metal into a semiconductor. *Phys. Rev. B.* **64**, 184420 (2001).
33. Sun, J. Z., Brown, S. L., Chen, W. *et al.* Spin-torque switching efficiency in CoFeB-MgO based tunnel junctions. *Phys. Rev. B.* **88**(10), 104426 (2013).
34. Aharoni, A. Demagnetizing factors for rectangular ferromagnetic prisms. *J. Appl. Phys.* **83**(6), 3432–3434 (1998)
35. Sato, H., Enobio, E. C. I., Yamanouchi, M. *et al.* Properties of magnetic tunnel junctions with a MgO/CoFeB/Ta/CoFeB/MgO recording structure down to junction diameter of 11 nm. *Appl. Phys. Lett.* **105** (6), 062403 (2014)
36. Nagashio, K., Nishimura, T., Kita, K. & Toriumi, A. Contact resistivity and current flow path at metal/graphene contact. *Appl. Phys. Lett.* **97**(14), 143514 (2010).
37. Liao, A. D., Wu, J. Z., Wang, X. *et al.* Thermally limited current carrying ability of graphene nanoribbons. *Phys. Rev. Lett.* **106**(25), 256801.
38. Blech, I. A. Electromigration in thin aluminum films on titanium nitride. *J. Appl. Phys.* **47**(4), 1203–1208 (1976).
39. Wang, P. C., Filippi, R. G. Electromigration threshold in copper interconnects. *Appl. Phys. Lett.* **78**(23), 3598–3600 (2001).

40. Steinhögl, W., Schindler, G., Steinlesberger, G. *et al.* Comprehensive study of the resistivity of copper wires with lateral dimensions of 100 nm and smaller. *J. Appl. Phys.* **97**(2), 023706 (2005).
41. Behin-Aein, B., Sarkar, A., Srinivasan, S. *et al.* Switching energy-delay of all spin logic devices. *Appl. Phys. Lett.* **98**(12), 123510 (2011).

Acknowledgements

This work is supported by China Scholarship Council (CSC), the Innovation Foundation of Beihang University (BUAA) for PhD Graduates, and French project ANR-MARS, ANR-DIPMEM, PEPS-NVCPU. The authors thank Qi AN and Zhaohao WANG for fruitful discussions. W.S.Z. thanks the support by the National Natural Science Foundation of China (Grant No.61571023).

Author Contributions

W.S.Z. and A.F coordinated the proposal and supervised the project. L.S. developed the model and made the calculation. L.S., W.S.Z., Y.G.Z., J.O.K. and A.F. analyzed the data. L.S., W.S.Z., Y.Z., A.B. and A.F. edited the manuscript. All authors reviewed and commented the manuscript.

Additional Information

Competing financial interests: The authors declare no competing financial interests.

How to cite this article: Su, L. *et al.* Current-limiting challenges for all-spin logic devices. *Sci. Rep.* **5**, 14905; doi: 10.1038/srep14905 (2015).



This work is licensed under a Creative Commons Attribution 4.0 International License. The images or other third party material in this article are included in the article's Creative Commons license, unless indicated otherwise in the credit line; if the material is not included under the Creative Commons license, users will need to obtain permission from the license holder to reproduce the material. To view a copy of this license, visit <http://creativecommons.org/licenses/by/4.0/>